Fuel 405 (2026) 136568

Contents lists available at ScienceDirect

Fuel

journal homepage: www.elsevier.com/locate/fuel

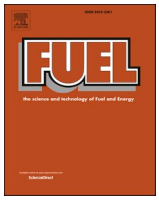

Full Length Article

Sulfur-doped carbon for enhanced flue gas desulfurization: Synergistic experimental and DFT insights

Jun Li [a], Xiang Wang [b], Xiao Zhu [c,g], Yuke Li [d], Min Yan [a,*], Yang Ma [a], Ping Cui [a], Jingcai Chang [e,f], Liqiang Zhang [g], Tao Wang [g], Chunyuan Ma [g], Zhanlong Song [g]

[a] School of Thermal Engineering, Shandong Jianzhu University, Jinan 250101 Shandong, China
[b] Institute of Process Engineering, Chinese Academy of Science, Haidian 100190, Beijing, China
[c] State Key Joint Laboratory of Environment Simulation and Pollution Control, School of Environment, Tsinghua University, Beijing 100084, China
[d] Department of Water Management, Faculty of Civil Engineering and Geosciences, Delft University of Technology, Stevinweg 1, 2628 CN Delft, the Netherlands
[e] School of Environmental Science and Engineering, Shandong University, Qingdao 266237 Shandong, China
[f] WeiHai Research Institute of Industrial Technology of Shandong University, Weihai, Shandong 264209, China
[g] School of Energy and Power Engineering, Shandong University, Jinan, Shandong 250061, China

ARTICLE INFO

Keywords:
Sulfur-doped activated coke
Physicochemical properties
Enhanced desulfurization mechanism
DFT calculations

ABSTRACT

The synthesis of sulfur-doped activated coke (SAC) using SO_2 as an activator enables simultaneous desulfurizer production and sulfur resource utilization. This study systematically investigated the evolution of carbon properties through sulfur doping and the enhanced desulfurization mechanism through experiments and density functional theory (DFT) calculations. The results demonstrated that SO_2 was primarily converted to elemental sulfur (maximum yield: 92.17 %) via redox reactions with carbon, while doped sulfur mainly existed as thiophene and oxidized sulfur groups (maximum doping: 18.92 wt%). Surface sulfur doping modified carbon's physicochemical properties and produced unique saddle-shaped SO_2 adsorption curves. Transient experiments and DFT calculations revealed enhanced hydrophilicity through strengthened H_2O interactions with sulfur-containing groups (the maximum adsorption energy of H_2O reached −58.70 kJ/mol, 2.64 times that of pristine sulfur-free carbon), which promoted H_2SO_4 migration in micropores via concentration-gradient diffusion to enhance desulfurization. This work provided both a waste-to-resource strategy for desulfurizer preparation and atomic-level insights into the desulfurization enhancement mechanism of SAC, offering design principles for advanced carbon materials in flue gas purification.

1. Introduction

Thermal power generation is a key component of China's energy structure. Therefore, environmental issues arising from coal combustion require continuous solution optimization [1]. While calcium-based wet flue gas desulfurization remains the predominant technology for large-scale applications, its well-documented challenges—including high water consumption [2], and difficulties in desulfurization gypsum utilization [3]—motivate exploration of complementary approaches. In contrast, dry flue gas desulfurization using porous activated coke (AC) as an emerging alternative offers potential advantages such as adsorbent recyclability [4], near-zero wastewater discharge, and the ability to convert SO_2 into value-added sulfur products [4], particularly in water-scarce regions or for resource recovery purposes.

Desulfurization using AC is a complex gas–solid heterogeneous catalytic reaction ($SO_2 + 0.5O_2 + H_2O \rightarrow H_2SO_4$), generally comprising several stages: channel transportation, SO_2 adsorption, catalytic oxidation, hydration, and migration of H_2SO_4 products. The physicochemical properties of AC, such as pore structure and surface functional groups, significantly influence the microscopic behavior of gas molecules and the desulfurization performance. Therefore, adjusting these properties to enhance desulfurization activity has become a research focus. Pores provide molecular transport and reaction sites throughout the process, which are necessary for AC to exhibit high activity. The size differences of the adsorbate molecules led to different adsorption positions within the porous materials. It is generally believed that the optimal pore diameter for adsorption is 1.5 to 2 times the diameter of the adsorbate molecules [6]. The molecular diameters of SO_2, O_2, and H_2O in the flue gas components were approximately 0.411, 0.346, and 0.264 nm,

* Corresponding author.
E-mail address: yanmin19@sdjzu.edu.cn (M. Yan).

https://doi.org/10.1016/j.fuel.2025.136568
Received 14 May 2025; Received in revised form 12 August 2025; Accepted 17 August 2025
Available online 21 August 2025

Nomenclature

AC	activated coke
SAC	sulfur-doped activated coke
DFT	density functional theory
FTIR	Fourier transform gas analyzer
SEM	scanning electron microscopy
XRD	X-ray diffraction
XPS	X-ray photoelectron spectroscopy
E_{ad}	adsorption energy
$E_{comples}$	single-point energies of the adsorption complex
E_{H_2O}	single-point energies of H_2O
$E_{surface}$	single-point energies of the carbon
α	dimensionless parameter
β	dimensionless parameter
S_{BET}	specific surface area
S_{Mic}	micropore specific surface area
V_{Tot}	total pore volume
V_{Mic}	micropore volume
ESP	electrostatic potential
Y_{SO_2}	SO_2 yield
Y_{cos}	COS yield
Y_{CS_2}	CS_2 yield
Y_S	sulfur yield
$n^{in}_{SO_2}$	the molar amount of inlet SO_2
$n^{out}_{SO_2}$	the molar amount of outlet SO_2
n^{out}_{COS}	the molar amount of outlet COS
$n^{out}_{CS_2}$	the molar amount of outlet CS_2
Q_{ad}	SO_2 capacity
C_{in}	the inlet concentrations of SO_2
C_{out}	the outlet concentrations of SO_2
V_{ad}	gas flow rate
M_{SO2}	the molar mass of SO_2
m	AC mass
t	adsorption time
D	average pore size
vdW	van der Waals

respectively [7]. Therefore, micropores serve as reaction sites for SO_2 adsorption and catalytic oxidation [8]. The hierarchical pore structure, which includes micropores and meso/macropores, satisfies the requirements for adsorption and the migration and storage of H_2SO_4 products, thereby demonstrating enhanced adsorption performance [9,10].

Changing the chemical properties of the carbon surface through non-carbon heteroatom doping is a common method for enhancing the adsorption and catalytic oxidation of SO_2. Based on the properties of the doped atoms, they can be classified as into metals such as iron [11], copper [12], manganese [13], and vanadium [14], as well as non-metals such as oxygen, nitrogen, and sulfur. According to the literature, metal atom doping enhances desulfurization activity when combined with SO_2 to form thermally stable sulfates [15], ultimately leading to poisoning and deactivation of the metal heteroatoms. Conversely, nonmetallic doping offers economic and sustainability advantages [16]. For example, epoxy functional groups serve as active sites for the oxidation of SO_2 [17], and the presence of hydroxyl groups (–OH) can enhance SO_2 adsorption through hydrogen bonding interactions and lower the reaction energy barrier for the oxidation of SO_2 to SO_3 by epoxy groups [18]. Ketone groups (O–C(3)–O) can directly activate O_2, facilitating the direct oxidation of SO_2 by nondissociative oxygen [19]. Nitrogen-doping enhances non-covalent interactions with SO_2 by altering the electrostatic distribution on the carbon surface [20,21]. Based on experiments and density functional theory (DFT) calculations, sulfur-doping exhibits a similar effect by inducing carbon structural distortions and altering the surface polarity [22,23], thereby changing the charge transfer characteristics and interactions with adsorbates. Surface sulfur functionalization confers carbon enhanced electrochemical performance [24] and remarkable gas storage capacity for H_2/CO_2 [25]. Exploring the convenient and economical synthesis of non-metallic heteroatom-doped carbon materials is the key to achieving promotion and industrial applications.

The efficient utilization of high-concentration SO_2 (5–15 % [26]) released during the thermal regeneration reaction ($C + 2H_2SO_4 \rightarrow 2SO_2 + CO_2 + 2H_2O$) of SO_2-saturated AC is a prerequisite for achieving sulfur resource recovery. The carbothermal reduction method is commonly used to convert SO_2 into elemental sulfur ($C + SO_2 \rightarrow S + CO_2$) [27]; however, the redox interaction between C-SO_2 induces further development of carbon pores and achieves surface sulfur doping [28]. To address this research gap, our previous research demonstrated the feasibility of using SO_2 as an activator to prepare highly active sulfur-doped carbon materials for desulfurization applications [29], which promotes the coupling of adsorbent preparation and sulfur resource utilization processes and is of great significance for simplifying the process. Nevertheless, the fundamental mechanisms governing the superior desulfurization activity of sulfur-functionalized carbon materials in simulated flue gas environments, especially the atomic-level understanding of their distinctive dynamic adsorption behaviors, are still not fully elucidated and demand comprehensive study.

To fill this knowledge gap, the purpose of this study is to reveal the reaction mechanism of sulfur-doped carbon materials prepared by SO_2 activation for enhanced desulfurization. Experiments were arranged at different SO_2 activation times, and the physicochemical properties of the collected sulfur-doped activated coke (SAC) samples were fully characterized. The influence of flue gas components on the SO_2 adsorption performance of SAC was revealed through SO_2 dynamic adsorption testing and DFT calculations, and the reaction mechanism for enhancing desulfurization was summarized.

2. Experimental and computational details

2.1. Synthesis of carbon materials with sulfur doping

The sulfur-doped carbon materials used in this study were synthesized using the carbothermal reduction method with SO_2 (known as SO_2 activation). The carbon-rich precursor was derived from the fuel coal used at the Guoneng Shengli Power Plant, and the raw material composition is detailed in Table S1. Before formal experiments, the coal was crushed and sieved to a particle size of 80 to 150 mesh (average diameter of approximately 140 μm) and dried under a vacuum at 80 °C for 12 h, after which it was collected and stored in a drying dish for future use. The preparation of SAC involves several key processes such as pyrolysis, demineralization, drying, and SO_2 activation, as illustrated in Fig. 1a.

Pyrolysis involves heating a specific mass of coal powder in a N_2 atmosphere (flow rate of 500 mL/min) to 700 °C at a constant rate of 10 °C/min, maintained for 0.5 h, followed by natural cooling to room temperature. This process removed most of the moisture and volatiles from the coal particles, resulting in coke with an initial porous structure. To eliminate the influence of mineral matter in the ash on subsequent reactions, pyrolytic coke was mixed with 2 mol/L HCl and HF solutions at a mass ratio of 1:20. The mixture was magnetically stirred at 60 °C for 12 h. The demineralized coke was washed with deionized water until it became neutral. Subsequently, it was deeply dehydrated in a vacuum at 110 °C for 12 h and collected for future use.

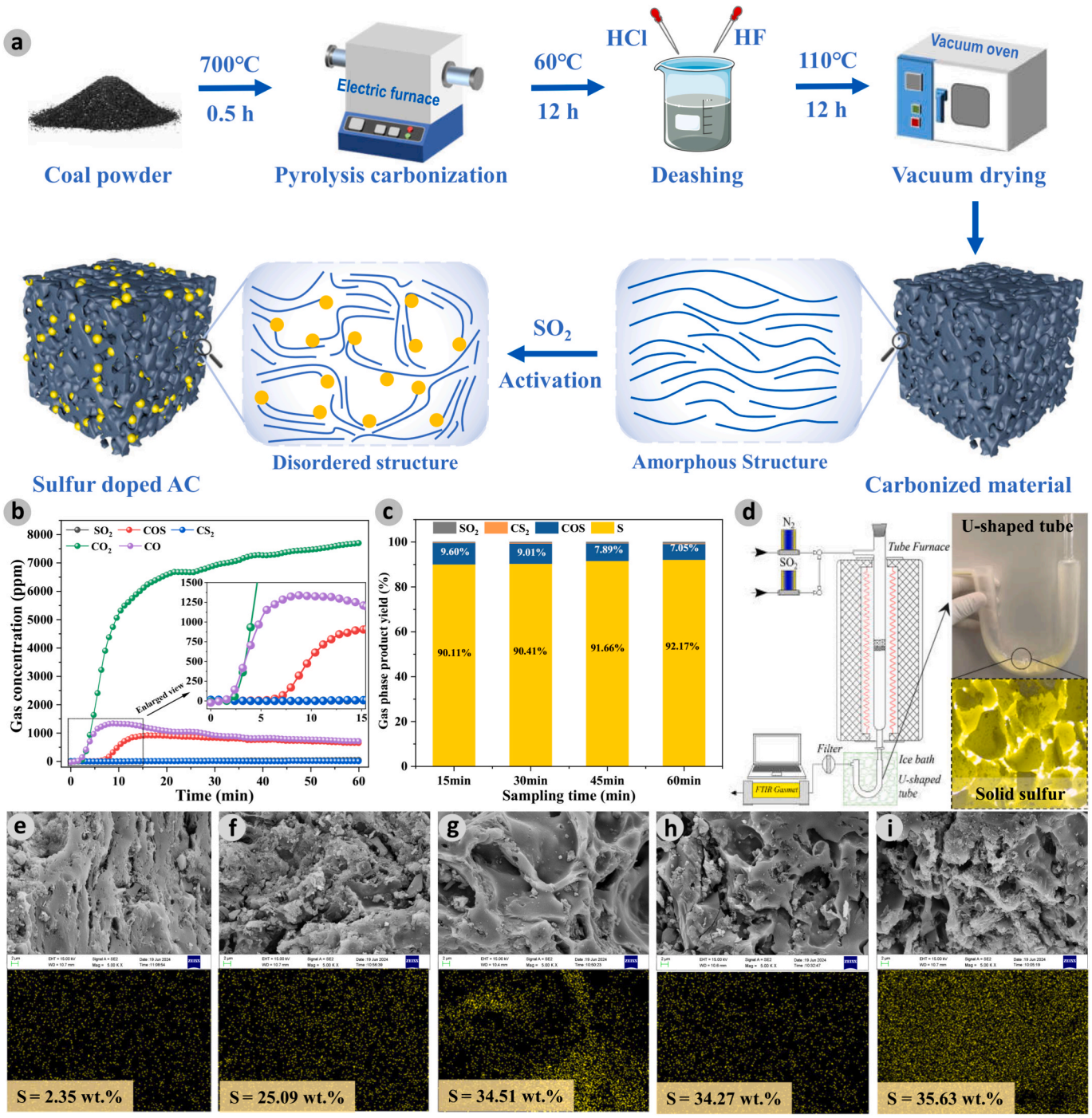

Fig. 1. Preparation process of sulfur-doped activated coke (SAC) and characterization of gas–solid products. (a) Schematic of SO_2 activation method for preparing SAC. (b) Time-dependent curve of gas-phase products generated at 800 °C (enlarged view: concentration curve within 1500 ppm during the first 15 min of reaction). (c) Yield distribution of sulfur-containing products at different reaction times. (d) Schematic of SAC preparation device (enlarged view: U-shaped condenser and collected solid sulfur). SEM and sulfur distribution maps of (e) de-ashed coke, (f) SAC-A15, (g) SAC-A30, (h) SAC-A45, and (i) SAC-A60.

Finally, using the fixed-bed experimental setup shown in Fig. 1d, the obtained coke was activated with SO_2 to prepare SAC. The reaction occurred in a quartz reaction tube (inner diameter of 30 mm, length of 1000 mm), and the temperature was precisely controlled using an electric heating furnace. The demineralized sample (2 g) was heated in a N_2 atmosphere to a target temperature of 800 °C (flow rate of 200 mL/min). Subsequently, the gas was switched to a mixture containing 10 vol % SO_2 and the reaction time was controlled between 15 and 60 min. The exhaust gases were condensed and filtered through an ice bath, and the concentrations of the gas-phase products were monitored in real time using a Fourier transform gas analyzer (FTIR; Dx4000, Finland), with measurements taken every 5 s. To protect the measuring instrument, the exhaust gas was diluted with 1800 mL/min N_2. Upon completion of the reaction, the gas flow was switched back to N_2, and the reaction tube was quickly removed from the furnace for cooling. The collected samples were then sealed and stored to prevent direct exposure to the air. The samples were labeled as SAC-A*x*, where "*x*" represents the activation time with SO_2. The following parameters were used to evaluate the yield of sulfur-containing gas.

$$Y_{SO_2} = n^{out}_{SO_2}/n^{in}_{SO_2} \times 100\% \quad (1)$$

$$Y_{cos} = n^{out}_{COS}/n^{in}_{SO_2} \times 100\% \quad (2)$$

$$Y_{CS_2} = 2n^{out}_{CS_2}/n^{in}_{SO_2} \times 100\% \quad (3)$$

$$Y_S = 100\text{-}Y_{SO_2}\text{-}Y_{COS}\text{-}Y_{CS_2} \quad (4)$$

where $n^{in}_{SO_2}$ (mol) is the molar amount of SO_2 at the reactor inlet and, $n^{out}_{SO_2}$, n^{out}_{COS}, and $n^{out}_{CS_2}$ (mol) are the molar amounts of SO_2, COS, and CS_2 at the outlet, respectively. Y_{SO_2}, Y_{cos}, Y_{CS_2}, and Y_s (%) are the SO_2, COS, CS_2, and sulfur yields, respectively.

2.2. SO_2 dynamic adsorption performance test

The dynamic SO_2 adsorption performance of the SAC was evaluated under simulated flue gas conditions using the fixed-bed setup shown in Fig. S1. The entire setup consisted of a mixed gas preparation system, fixed-bed adsorption unit, and exhaust gas testing system. The total gas flow was controlled at 200 mL/min, with 500 ppm SO_2, 6 % O_2, 8 % H_2O, and N_2 as the balance gas. Each experiment used 0.2 g of SAC sample, with adsorption temperature and duration set at 75 °C and 2 h, respectively. The gas analyzer continuously monitored the exhaust gas concentrations, allowing the adsorption breakthrough curve to be plotted based on time-dependent changes in the SO_2 concentration. The SO_2 adsorption capacity of the carbon was calculated using the following formula:

$$Q_{ad} = \int_0^t ((C_{in}\text{-}C_{out}) \times 10^{-6} \times V_{ad} \times M_{SO_2}/V_m)dt/m \quad (5)$$

where Q_{ad} (mg/g) is the SO_2 capacity; C_{in} and C_{out} (ppm) are the inlet and outlet concentrations of SO_2, respectively; t (min) is the time; V_{ad} (mL/min) is the gas flow rate; M_{SO2} (64 g/mol) is the molar mass of SO_2; and m (g) is the AC mass before adsorption.

2.3. Structural characterization

The microscopic morphology and surface elemental maps were obtained using scanning electron microscopy (SEM) (SUPARA™55, Carl Zeiss, Oberkochen, Germany) and energy-dispersive spectroscopy. The pore structure characteristics of the samples were obtained by N_2 adsorption–desorption at 77 K (Autosorb1-C, Quantachrome, USA). The surface area was obtained using the BET calculation method, and the pore distribution characteristics were calculated based on solid DFT. Raman spectroscopy (Raman) analysis was performed on a micro-Raman spectrometer (PERS-SR532) using an argon-ion laser with a wavelength of 572 nm as the light source. X-ray diffraction (XRD) (Miniflex 600X, Tokyo, Japan) of Cu-Kα radiation source was used to analyze the crystal phase composition (40 kV, 10–90°, scan rate 2°/min). X-ray photoelectron spectroscopy (XPS) analysis was performed using an ESCALAB 250XL instrument from Thermo Scientific (MA, USA) to investigate the chemical structure, utilizing an Al-Kα X-ray source with a photon energy of 1486.6 eV. The steam adsorption instrument (BELSORP-maxll, Microtrac, Osaka, Japan) was used to measure the adsorption performance at 25 ℃.

2.4. DFT simulation and analysis

Theoretical calculations of the weak interactions between carbon models containing different sulfur functional groups and H_2O molecules were conducted using Gaussian 16 software. To effectively mitigate the edge effects-induced non-convergence of adsorption energy caused by finite model size and enhance the reliability of carbon-based models in DFT calculations [20], this study employs a carbon cluster model containing 19 benzene rings to simulate the carbon matrix. Based on the XPS analysis results of sulfur-containing functional groups on the carbon after SO_2 activation in this study, three representative sulfur-functionalized carbon cluster models were constructed to investigate interactions with adsorbate molecules (namely thiophene, sulfoxide, and sulfone groups). Geometry optimization and vibrational frequency calculations were performed at the M06-2X/6-31G(d,p) level, considering the basis set superposition error through geometrical and dispersion corrections [30]. To evaluate the adsorption energy E_{ad}, the single-point energy of the optimized carbon surface model was calculated at the M06-2X/6-311+G(d,p) level. The multifunctional wave function analysis program Multiwfn was combined with a VMD visualization tool to analyze electrostatic potential and noncovalent interactions [31,32]. E_{ad} was determined as follows:

$$E_{ad} = E_{comples}\text{-}(E_{H_2O} + E_{surface}) \quad (6)$$

where E_{H_2O}, $E_{surface}$, and $E_{comples}$ (kJ/mol) represent the single-point energies of the isolated H_2O molecules, the carbon surface, and the adsorption complex, respectively.

The reliability of DFT methodology was validated through comparative thermodynamic calculations for SO_2 using both Gaussian (M06-2X/6-311+G(d,p)) and FactSage commercial packages. As shown in Fig. S2, the computed enthalpy differences (H(T)-H(T = 298 K)) and entropy values exhibited remarkable consistency between both methods [33], with maximum deviations limited to 1.74 % for enthalpy differences and 0.31 % for entropy. This excellent agreement conclusively demonstrates the reliability of the computational approach.

3. Results and discussion

3.1. Preparation and structural characterization

Based on our previous findings [29], sulfur doping is a key factor in enhancing the adsorption performance of carbon materials. Therefore, the objective of this study was to elucidate the interactions between SAC preparation, physicochemical properties, and enhanced desulfurization mechanisms. Considering the complexity of the C-SO_2 reaction and the various byproducts, effective control over the types and quantities of sulfur functional groups loaded onto the carbon was realized by varying the activation reaction time of SO_2. According to the preparation process and methods described in Fig. 1a and Section 2.1, the reaction temperature was fixed at 800 °C, with reaction times set to 15, 30, 45, and 60 min to obtain SACs with varying degrees of activation.

The distribution of the gaseous products during SO_2 activation over time is shown in Fig. 1b. The SO_2 concentration in the exhaust gas was nearly zero, indicating that SO_2 was almost completely converted under reaction conditions. The primary gas product was CO_2, which partially underwent a Boudouard reaction with carbon to form CO. According to the literature [34], CO can directly react with the intermediate product C(S) to generate COS, making COS the main non-target sulfur-containing byproduct. COS exhibits strong reducing properties and readily reacts with SO_2 to produce sulfur in the presence of carbon as a catalyst [5]. Therefore, COS and SO_2 generally do not coexist in the gaseous phase. Based on the instantaneous concentration distribution of the product at a predetermined reaction time, the yields of the sulfur-containing gases were obtained using Eqs. (1)–(4), and the corresponding parameters are presented in Fig. 1c and Table S2. The sulfur yield Y_S increased with increasing reaction time, ranging from 90.11 % to 92.17 %. The sum of the yields of sulfur and COS ($Y_S + Y_{COS}$) exceeded 99 %, indicating that these were the main products of the carbothermal reduction of SO_2. As shown in Fig. 1d, a large amount of solid sulfur, which has been widely used as a raw chemical material, was deposited and collected in a U-shaped condenser immersed in an ice bath after the experiment.

The pyrolysis and demineralization processes can lead to the formation of porous structures in the sample, along with a limited distribution of sulfur, as illustrated by the SEM-EDX results shown in Fig. 1e.

With increasing SO_2 activation time, wrinkles and numerous new pores appeared on the carbon surface, thereby increasing the disorder of the carbon (Fig. 1f–1i). These characteristics can significantly enhance the mass transfer and catalytic efficiency of desulfurization. The surface sulfur content increased with the activation time, reaching a maximum of 35.63 wt% after 60 min of reaction in the tested area (SAC-A60, Fig. 1i). The pore development caused by SO_2 activation and sulfur-containing groups formed by sulfur doping are described in detail in the following sections.

3.2. Characterization of physicochemical properties of SAC

The influence of SO_2 activation on the physicochemical properties of carbon can be comprehensively understood by analyzing its crystal structure, pore characteristics, and surface functional groups. Fig. 2a shows the XRD pattern, with distinct peaks at 23.4 and 44.2°, representing the (002) and (100) planes of graphitic carbon, respectively [35–37]. The peak intensity decreased significantly with increasing activation time, indicating a decrease in the content of ordered graphite carbon. Fig. 2b shows the Raman spectrum, where the D-band at 1360 cm^{-1} is related to carbon defects and the G-band at 1580 cm^{-1} corresponds to the sp^2 graphite structure [38]. The integrated strength ratio of the D-band to the G-band (I_D/I_G) is commonly used to indicate the degree of carbon crystallization. The increase in the I_D/I_G ratio with extended SO_2 activation suggested that the carbon structure experienced greater disorder and a reduction in crystallinity. The above analysis indicates that prolonged activation may introduce more defects into the carbon matrix, potentially enhancing the surface area and reactivity of the material.

Fig. 2c illustrates the N_2 adsorption–desorption isotherm, displaying typical I/IV type characteristics, indicating that the carbon material has a hierarchical pore structure with micropores, mesopores, and macropores. Compared to the pristine coke, SAC-A15 showed a slight decrease in N_2 adsorption, suggesting that the initial SO_2 activation occupied some pores owing to its interaction with active sites on the carbon surface. However, the subsequent significant increase in N_2 adsorption indicated that SO_2 activation continuously promoted pore development, enhancing the overall porosity of the material. The detailed pore structure parameters are listed in Table 1. The specific surface area and pore volume integral of SAC-A60 reached the maximum values of

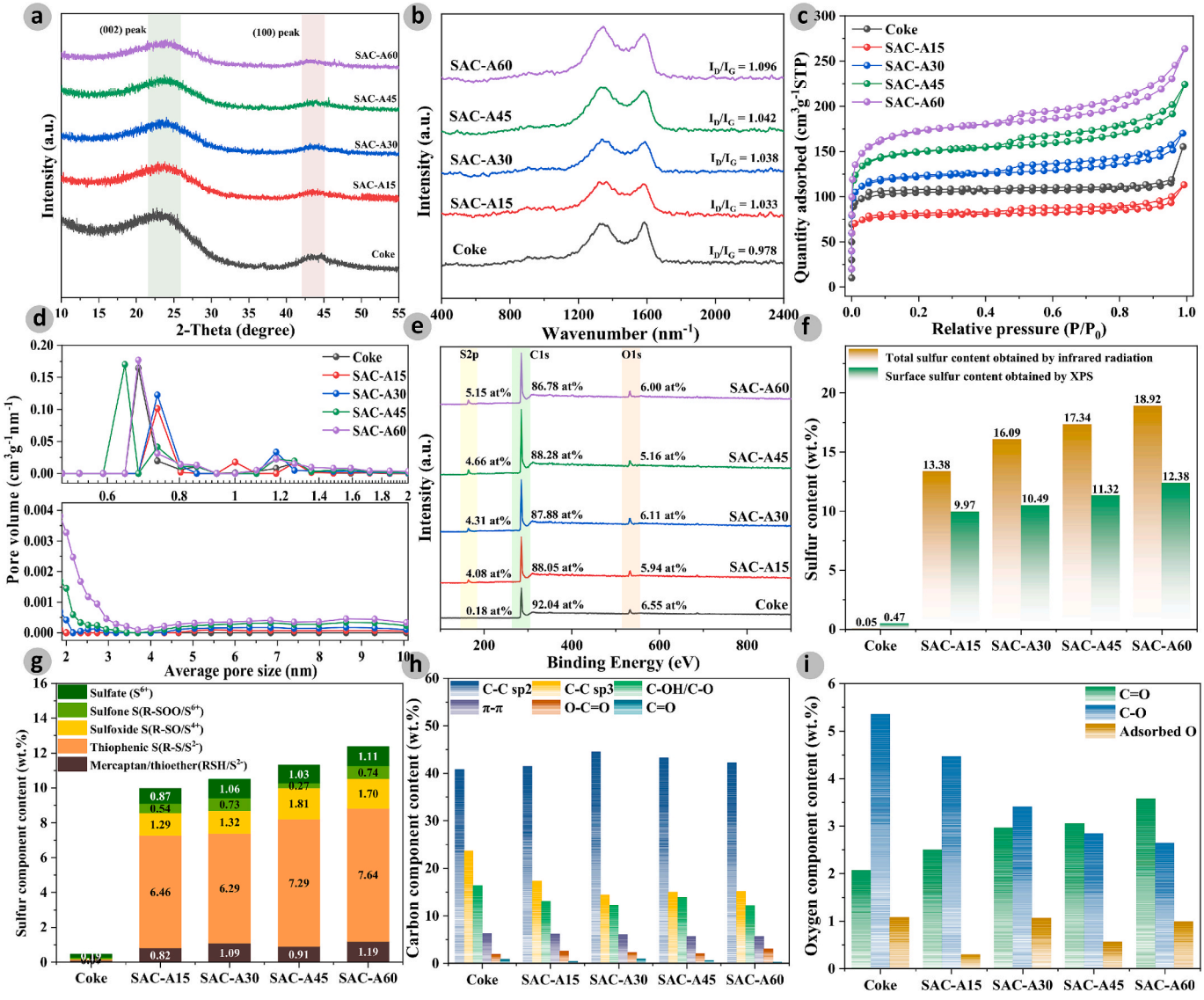

Fig. 2. Physicochemical properties of SAC. (a) XRD patterns, (b) Raman spectra, (c) N_2 adsorption–desorption isotherms, (d) pore structure characteristics, and (e) overall XPS spectra of pristine coke, SAC-A15, SAC-A30, SAC-A45, and SAC-A60. (f) Sulfur content measured by XPS and infrared sulfur analyzer. Distributions of (g) sulfur, (h) carbon, and (i) oxygen functional groups of pristine coke, SAC-A15, SAC-A30, SAC-A45, and SAC-A60.

Table 1
Pore structure characteristics of activated cokes prepared in SO_2 atmospheres.

ACs	S_{BET}	S_{Mic}	V_{Tot}	V_{Mic}	D
Coke	307.80	271.22	0.240	0.145	3.122
SAC-A15	241.69	211.23	0.175	0.109	2.895
SAC-A30	374.39	307.50	0.263	0.159	2.810
SAC-A45	447.32	350.03	0.347	0.188	3.101
SAC-A60	537.33	374.51	0.408	0.194	3.036

S_{BET}: specific surface area (m^2/g), S_{Mic}: micropore specific surface area (m^2/g), V_{Tot}: total pore volume (cm^2/g), V_{Mic}: micropore volume (cm^2/g), D: average pore size (nm).

537.33 m^2/g and 0.408 cm^2/g, respectively. To further elucidate the impact of the SO_2-C reaction on the pore structure, the micropore and mesopore structural parameters of the pristine coke and SACs are illustrated in Fig. S3. The dimensionless α and β are defined as the ratios of the differences in mesopore/macropore and micropore values between the pristine coke and SACs ($\alpha = \Delta S_{Mes/Mac}/\Delta S_{Mic}$; $\beta = \Delta V_{Mes/Mac}/\Delta V_{Mic}$), respectively. For the SAC-A15, the α and β values were 0.1 and 0.81, respectively, indicating that the reduction in micropores was greater than that in mesopore/macropores, suggesting that SO_2 molecules mainly occupied the microporous structure in the early stages of the reaction. Within the 30–60 min range of SO_2 activation, the pore parameters of the SACs were further improved, with the α and β values increasing from 0.84 to 1.22 and 0.69 to 2.44, respectively. This suggests that as the reaction deepens, the development of mesopore/macropore is promoted, and the SO_2 activation shifts gradually from "pore creation" to "pore expansion." The pore distribution graph shown in Fig. 2d confirms this conclusion, as the intensity of the mesoporous peak in the range of 2–10 nm [39] gradually increases with increasing activation time.

Fig. 2e presents the overall XPS spectrum, where carbon, oxygen, and sulfur are the primary elements. With prolonged activation time, the oxygen content of the pristine coke and SACs fluctuated within a certain range, whereas the sulfur atom counts gradually increased and the carbon content decreased. The sulfur content measured using the infrared sulfur analyzer (for the total amount) was similar to the XPS value (for surface characterization) and showed a similar trend, indicating that SO_2 activation primarily led to sulfur doping on the carbon surface (Fig. 2f). The S2p spectrum was deconvoluted to compare the distribution of sulfur species in the SACs, as shown in Fig. S4a. Electrons in the S2p orbitals undergo energy-level splitting under X-ray excitation, leading to the appearance of double peaks in the spectra of 2p3/2 and 2p1/2, which exhibit a binding energy difference of 1.18 eV. The area ratio of the two peaks was set to 2:1, with an equal full width at half maximum for both peaks [26]. The binding energies for the S2p3/2 orbitals at 162.5, 164.1, 166, 168, and 169.5 eV corresponded to mercaptan (−SH), thiophene (–S–), sulfoxide (−SO), sulfone (−SOO), and sulfate species, respectively [40,41]. Based on the results shown in Fig. 2f and Fig. S4a, the types and quantities of sulfur-containing groups in the samples are shown in Fig. 2g. The activation of SO_2 leads to the formation of a substantial amount of thiophene-type sulfur on the carbon surface, and the quantity of each sulfur-containing group increased noticeably as the activation time increased. The C1s and O1s spectra were deconvoluted (Figs. S4b and S4c) to determine the distributions of carbon and oxygen-containing functional groups [42–44], with the corresponding results presented in Fig. 2h and 2i and detailed parameters listed in Tables S3 and S4. The content of unsaturated hydrogen defects, represented by C–C sp3 hybridized carbon, decreased with increasing degree of activation, suggesting that these sites may be gradually consumed as active sites. Additionally, an increase in the C=O content was observed along with a decrease in the C-O content (Fig. 2i), likely due to the strengthening of the SO_2-C reaction, which increased the quantity of decarboxylation reaction intermediates [45]. These results indicate that SO_2 as an activator reshapes the physicochemical properties of carbon and that these changes affect the subsequent desulfurization process.

3.3. SO_2 dynamic adsorption tests

To elucidate the impact of changes in the physicochemical properties of SAC on the low-temperature desulfurization performance, a series of dynamic SO_2 adsorption tests were conducted according to the method described in Section 2.2. Fig. 3a shows the SO_2 adsorption breakthrough curves for the pristine coke and SACs. The curve characteristics of the pristine coke are consistent with those in the published literature [11,46,47]; that is, with an increase in adsorption time, the SO_2 concentration at the reactor outlet first sharply increased and then slowly increased. However, SACs exhibit a saddle-shaped characteristic, where the outlet SO_2 concentration shows a trend of first increasing, then decreasing, and then increasing again over time, which is inconsistent with the existing literature records. Additionally, as the degree of SO_2 activation increased, the peak intensity of outlet SO_2 significantly decreased within the first 10 min. According to the formula used to calculate the sulfur adsorption capacity (Eq. (5)), the closed area formed between the reactor inlet SO_2 concentration (C_{in} = 500 ppm) and breakthrough curve represents the effective adsorption area. This indicates that the SACs possessed a greater adsorption capacity than the pristine coke, as shown in Fig. 3b. After high-temperature pyrolysis and ash removal, the pores of the pristine coke developed well (Table 1) and exhibited SO_2 adsorption activity, with a calculated sulfur capacity of 21.21 mg/g. In contrast, the sulfur capacity of the SACs increased with increasing degree of activation, reaching a maximum value of 98.22 mg/g for SAC-A60. Combining Figs. 2g and 3b, there is a linear relationship between the number of sulfur-containing functional groups in the SAC and the sulfur capacity, particularly with sulfur oxides (such as sulfones and sulfoxides), as shown in Fig. S5. To increase the comparability of the experimental results, six types of AC were tested for SO_2 adsorption under the same experimental conditions: three commercial ACs (AY, XH, and FG) and three self-made ACs activated in oxygen and steam atmospheres (MD, ZD, and SL) [15]. The relevant parameters are listed in Tables S1 and S5. Fig. 3c shows that the SO_2 breakthrough curve characteristics of the six types of AC are similar to those of the pristine coke in Fig. 3a, and the sulfur capacity is generally smaller than that of the SACs (Fig. 3b). These results indicate that sulfur doping on the carbon surface through SO_2 activation enhances the low-temperature desulfurization performance and has unique dynamic adsorption characteristics.

The differences in the characteristics of the SO_2 breakthrough curves indicate that there are variations in the desulfurization reaction mechanism. To clarify the SAC desulfurization behavior under a flue gas atmosphere, transient experiments were conducted to determine the change in the outlet SO_2 concentration by continuously changing the inlet atmosphere [8]. Commercial FG and SAC-A30 were selected for comparison, with a blank condition serving as a reference. Each step lasted for 40 min, as shown in Fig. 3d and 3e. In step 1, only SO_2 was introduced, and FG achieved complete removal of SO_2 within the initial 5 min, whereas SAC-A30 rapidly failed and SO_2 quickly reached the inlet concentration (Fig. 3d). This indicated that under these conditions, the adsorption performance of SAC-A30 was inferior to that of FG. Subsequently, when only O_2 was introduced (step 2) and then only SO_2 was introduced again (step 3), no significant changes were observed for either material. This suggests that the oxygen pre-adsorbed on the carbon surface did not directly oxidize SO_2. Finally, when O_2 was included in the gas composition (step 4), the SO_2 concentration changed similarly for both adsorbents and decreased compared to the blank condition. However, the entire process did not exhibit the "saddle" feature. As shown in Fig. 3e, when switching from $SO_2 + O_2$ (step 2) to $SO_2 + H_2O$ (step 3), a noticeable decrease in the outlet SO_2 concentration was observed for both adsorbents. Introducing O_2 into the gas composition (step 4) enhances the desulfurization efficiency of SAC-A30 and FG, and SAC-A30 once again exhibited a saddle-shaped breakthrough curve

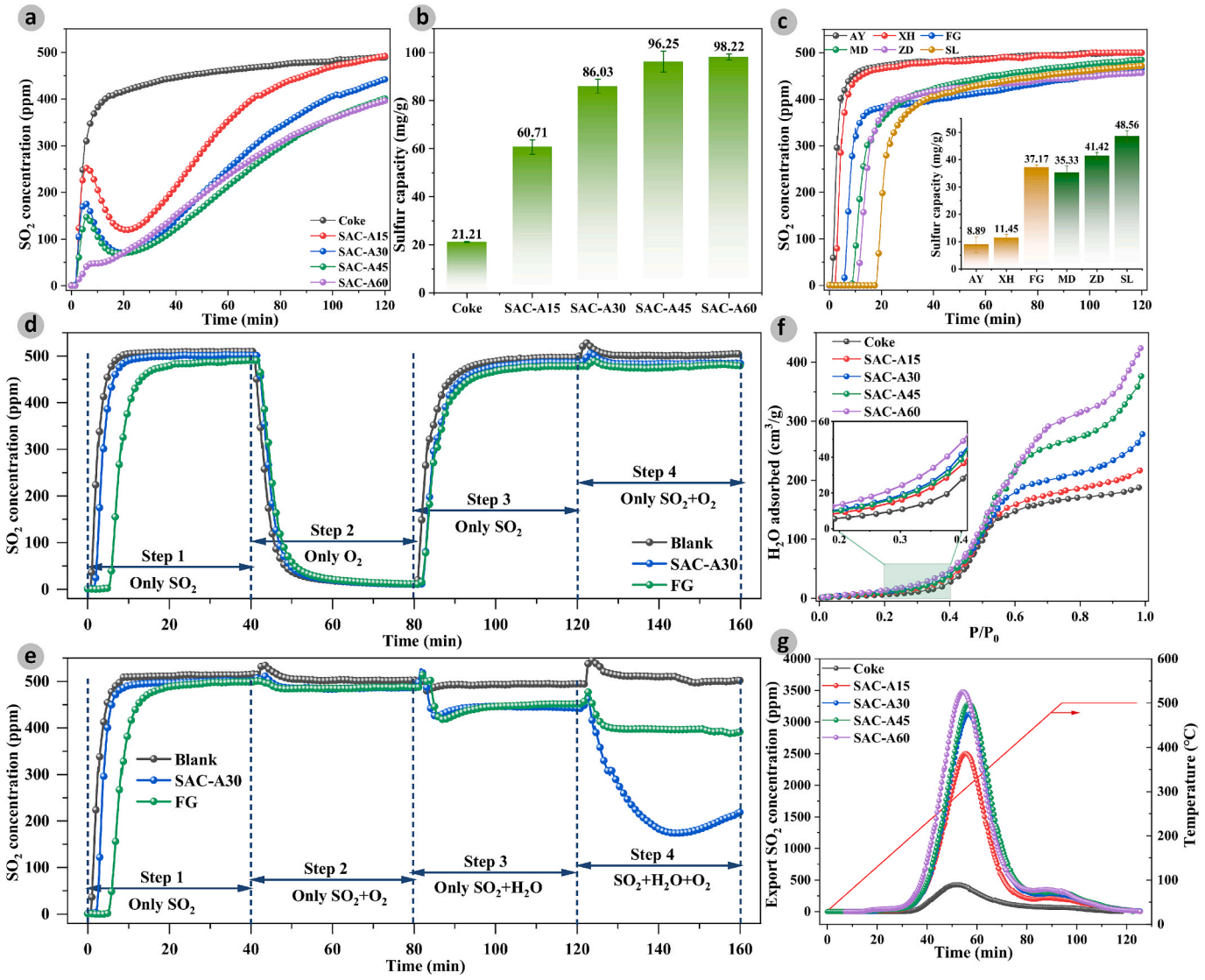

Fig. 3. SO_2 adsorption test of SACs. (a) SO_2 adsorption breakthrough curve and (b) cumulative sulfur capacity of pristine coke and SACs. (c) SO_2 adsorption test of six types of AC. Transient experiments of adsorption atmospheres of (d) SO_2, O_2, SO_2, $SO_2 + O_2$, and (e) SO_2, $SO_2 + O_2$, $SO_2 + H_2O$, $SO_2 + H_2O + O_2$. (f) Water vapor physisorption isotherms at 25 °C. (g) Programmed temperature desorption curve of adsorbed SACs (increase the temperature uniformly from 30 °C to 500 °C at 5 °C/min).

characteristic. These results indicate that H_2O has a significant promotional effect on the desulfurization reaction. Supplementary experiments were conducted to gain a deeper understanding of the promotion mechanism of H_2O, as shown in Fig. S6. After the introduction of H_2O (step 1) and $SO_2 + O_2 + H_2O$ (step 3), SAC-A30 did not exhibit sustained adsorption in the $SO_2 + O_2$ atmosphere (steps 2 and 4), ruling out the possibility of H_2O forming active intermediates with sulfur-containing groups.

Fig. 3f shows the water vapor physisorption isotherms of the pristine coke and SACs. The water vapor adsorption capacity of the SACs increased with increasing SO_2 activation time, thus exhibiting hydrophilicity. Although the pore structure parameters of SAC-A15 were smaller than those of the pristine coke, the surface sulfur doping enhanced the adsorption capacity of H_2O. Fig. 3g presented the temperature-programmed desorption profiles of SO_2 from the post-adsorption samples. The curves revealed that adsorbed SO_2 in micropores desorbed within the 200–500 °C range, with a maximum peak intensity centered at 300 °C. Sulfur doping increased the sulfur adsorption capacity of the carbon material, which was reflected in the stronger SO_2 desorption peak intensity and corroborated the adsorption results in Fig. 3a.

The results indicate that sulfur doping does not enhance the catalytic oxidation of SO_2 ($SO_2 + O \rightarrow *SO_3$). Conversely, its enhanced desulfurization mechanism is closely related to the presence of H_2O in the gas composition, particularly in the hydration process after SO_2 catalytic oxidation ($*SO_3 + H_2O \rightarrow *H_2SO_4$) and the product H_2SO_4 migration process (micropores → mesopores/macropores). However, robust evidence supporting the formation of a unified theory is still lacking.

3.4. DFT calculation of composite adsorption

Building on the experimental results presented above, DFT calculations were employed to further clarify the interactions between the H_2O molecules and sulfur-containing groups. A series of carbon-based models constructed from 19 benzene rings (doped with sulfur or undoped) was employed to simulate H_2O adsorption (Fig. S7 [29]). H_2O and SO_2 in the gas mixture are polar molecules, and the concentration of water vapor (8 vol%) is significantly higher than that of SO_2 (500 ppm). Although both gas molecules exhibited overall electrical neutrality, their internal charge distributions and geometric shapes imparted polar

characteristics. The electrostatic potential (ESP) distribution characteristics of SO_2 and H_2O molecules are illustrated in Fig. 4a and 4b, respectively. The oxygen atoms in the two molecules exhibit electron accumulation, resulting in electronegativity, whereas the sulfur and hydrogen atoms carry positive charges. Notably, the maximum electrostatic potential on the surface of the H_2O molecule is greater than that of the SO_2 molecule, suggesting that the polarity of H_2O is more pronounced. Compared with the pristine sulfur-free carbon (Fig. 4c), sulfur doping altered the local electron density and surface polarity (Fig. S6), thereby affecting their interactions with H_2O/SO_2 molecules. The influence of sulfur-containing groups on the adsorption of SO_2 was reported in our previous study [29] and is not elaborated here.

To further assess the impact of sulfur doping on H_2O physisorption, the edge adsorption configurations and corresponding adsorption energies were calculated (according to Eq. (6)). Additionally, colored isosurfaces and the corresponding spike values were utilized to reveal noncovalent interactions, as shown in Fig. 4d–4 g. The adsorption energy of the H_2O on the pristine carbon edge is –22.17 kJ/mol, with the isosurface between the oxygen atom (H_2O molecule) and the hydrogen atom (carbon edge) primarily shown in green, corresponding to a spike value of −0.01 a.u. (Fig. S8a), indicating that the interaction is mainly influenced by van der Waals (vdW) forces. The introduction of oxidized sulfur-containing groups (sulfone and sulfoxide) significantly increased the adsorption energy (Fig. 4e and 4f), reaching −54.73 and −58.70 kJ/mol respectively, with the maximum value being 2.64 times that of pristine sulfur-free carbon. The isosurface between the hydrogen atom (H_2O) and the oxygen atom (carbon edge) transitioned from dark green to blue, with spike values varying between −0.03 and −0.015 a.u. (Figs. S8b and c), indicating the formation of hydrogen bonds between the H_2O and sulfur-containing groups. The adsorption energy of the H_2O on the carbon edge doped with thiophene S was −28.3 kJ/mol, with the green equipotential surface (Fig. 4g) and spike position being < -0.01 a.u., suggesting that the H_2O physisorption was enhanced. The above calculation results indicate that sulfur doping significantly enhances H_2O physisorption, and the adsorption energy is markedly higher than that of SO_2 [29], indicating that H_2O molecules exhibit preferential adsorption near sulfur-containing groups.

The carbon models were also employed to investigate competitive SO_2 adsorption in the presence of pre-adsorbed H_2O, with Fig. 5 displaying the isosurface plots of H_2O/SO_2 co-adsorption configurations and ESP-colored vdW surface penetration maps for analyzing intermolecular electrostatic interactions. Fig. S9 showed the corresponding scatter plots of the density gradient versus sign(λ_2)ρ. The molecules formed stable trimer structures through cooperative adsorption on the carbon edge, with significant interpenetration of their vdW surfaces. The interpenetration distances quantitatively reflected the interaction strengths. For the pristine sulfur-free carbon (Fig. 5e), the vdW interpenetration distances measured 0.51 Å (carbon-H_2O) and 0.55 Å (carbon-SO_2), while the SO_2-H_2O intermolecular interpenetration distance of 1.11 Å revealed particularly strong electrostatic interactions, as confirmed by both the blue ESP isosurfaces (Fig. 5a) and the −56.84 kJ/mol adsorption energy. For sulfur-doped carbons, the interpenetration distance between the carbon and H_2O increased significantly, reaching a maximum of 1.5 Å for sulfone-doped carbon (Fig. 5g), confirming enhanced hydrophilicity. Conversely, the interpenetration distance between H_2O and SO_2 decreased (Fig. 5f–5 h), with a minimum of 0.72 Å (Fig. 5f), suggesting weakened electrostatic interactions. The adsorption energy of SO_2 on sulfoxide-doped carbon increased compared to that on pristine carbon due to the formation of an intermolecular hydrogen bond between the sulfur atom of SO_2 and the oxygen atom of the sulfoxide group, as indicated by the blue ESP isosurfaces (Fig. 5b). In contrast, the adsorption energies on the other two modified carbons decreased to –33.89 (Fig. 5c) and −38.00 kJ/mol (Fig. 5d), demonstrating that water pre-adsorption inhibited SO_2 adsorption on these surfaces.

A comparative analysis was performed to investigate the cooperative adsorption of dual H_2O and their intermolecular interactions with sulfur-containing groups, as illustrated in Fig. 6. The second H_2O consistently formed intermolecular hydrogen bonds with the pre-adsorbed H_2O, evidenced by the characteristic blue isosurfaces between water molecules (Fig. 6a-d) and interpenetration distances fluctuating between 0.95–1.03 Å (Fig. 6e-h). Notably, the adsorption energies of the second H_2O reached −53.46 and −51.57 kJ/mol for sulfone- and thiophene-doped carbons respectively, significantly exceeding those of SO_2 (–33.89 and −38.00 kJ/mol, Fig. 5). Combined with the dominant presence of thiophenic sulfur groups in SAC (Fig. 2g), these results demonstrate that under H_2O-preloaded conditions, SAC exhibits preferential adsorption of H_2O over SO_2.

In addition, the polar characteristics of H_2O molecules and formation of intermolecular hydrogen bonds facilitate their tendency to cluster.

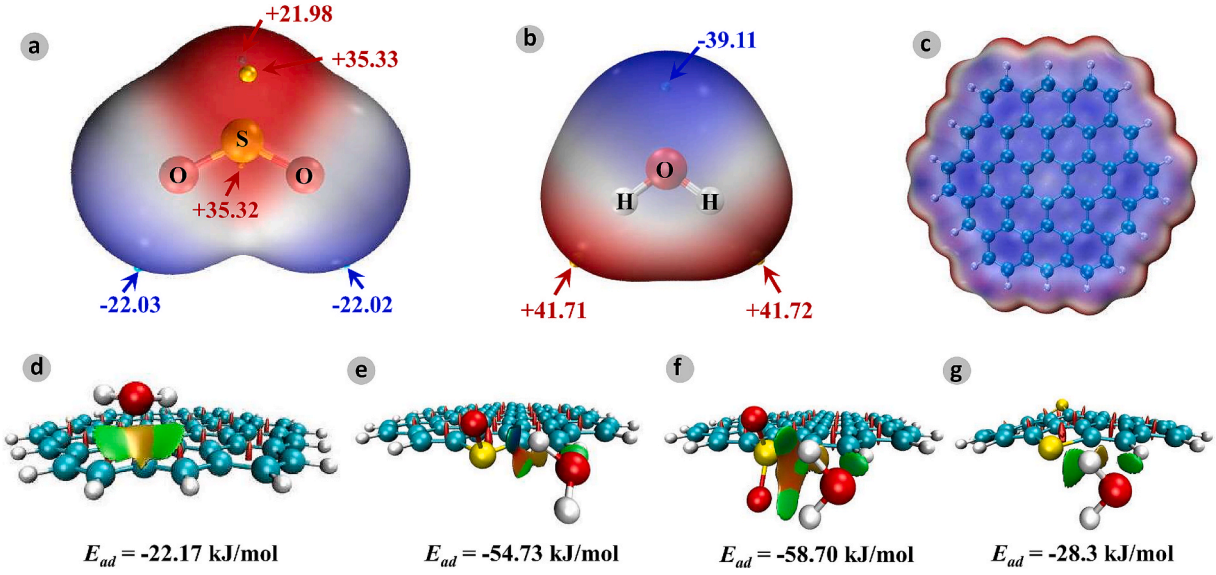

Fig. 4. Electrostatic potential maps of (a) SO_2, (b) H_2O, and (c) pristine carbon surface model (unit: kcal/mol). M06-2X/6-31G(d,p) gradient isosurfaces with $s = 0.5$ a.u. for the physisorption complexes, H_2O physisorption at the edge of the (d) pristine carbon, (e) near the sulfoxide S atom, (f) near the sulfone S atom, and (g) near the thiophene S atom.

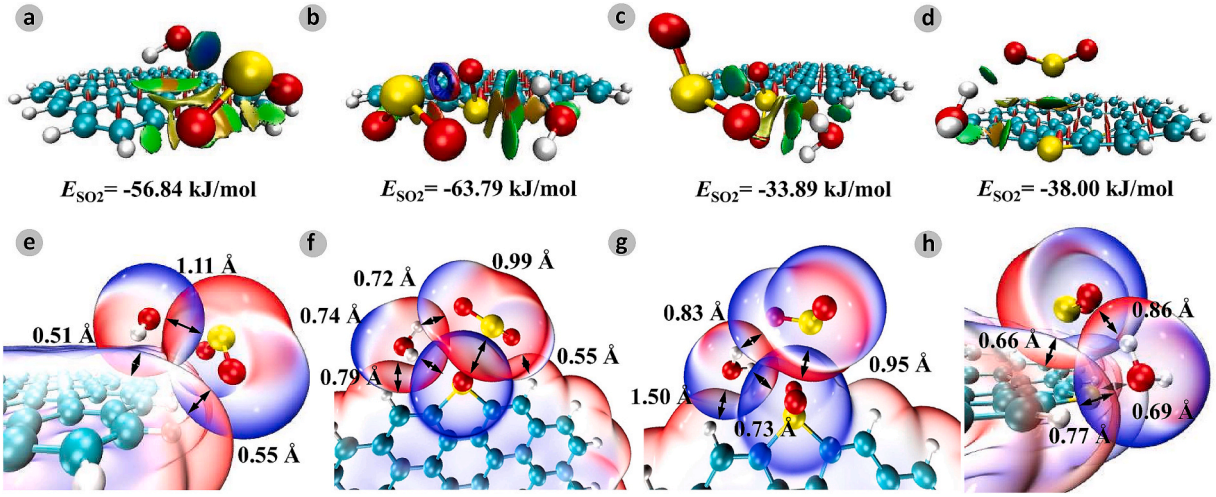

Fig. 5. Analysis of intermolecular interactions between sulfur-containing functional groups under competitive adsorption of H_2O and SO_2. (a), (e) pristine carbon; (b), (f) sulfoxide group; (c), (g) sulfone group; (d), (h) thiophene group.

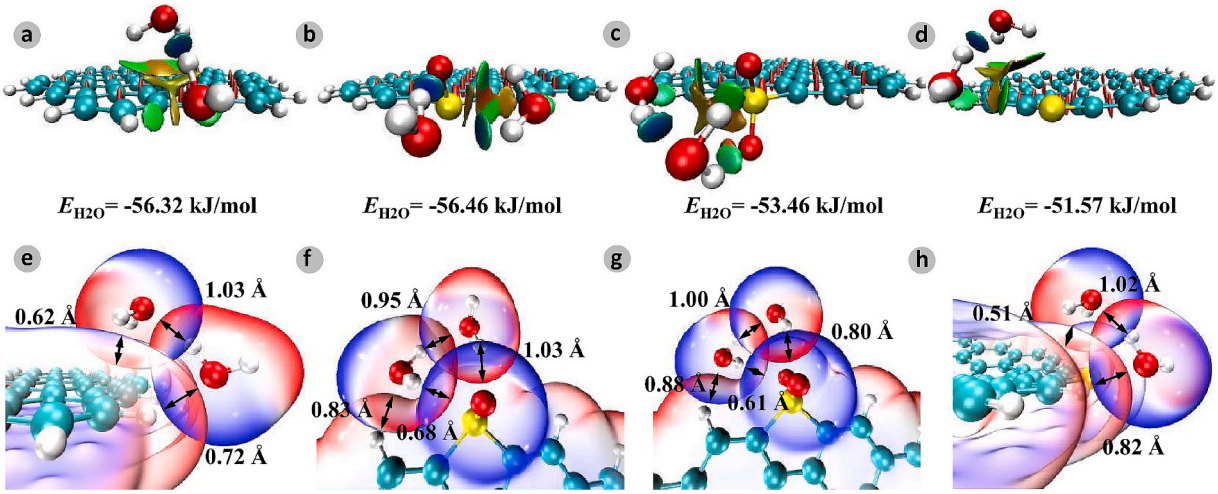

Fig. 6. Analysis of intermolecular interactions between dual H_2O co-adsorption and sulfur-containing functional groups. (a), (e) pristine carbon; (b), (f) sulfoxide group; (c), (g) sulfone group; (d), (h) thiophene group.

Based on the computational methods described in Section 2.4, the adsorption configurations and energies of the complexes containing multiple H_2O molecules were calculated, as shown in Fig. 7. The adsorption energy significantly increases with the increase of H_2O molecules, and the equipotential surfaces between the hydrogen and oxygen atoms are deep green and blue, corresponding to multiple peak positions below −0.02 a.u. (as shown in Fig. S10), further confirming that multiple H_2O molecules were prone to aggregation because of the formation of intermolecular hydrogen bonds. Thus, the sulfur-containing groups on the carbon surface significantly enhanced the ability to bind H_2O and promote aggregation, thereby exhibiting hydrophilicity, which corresponds to the experimental conclusion described in Fig. 3f.

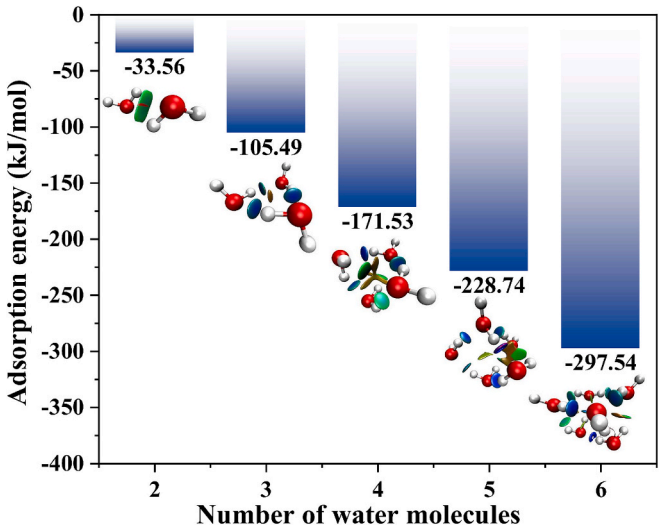

Fig. 7. Configuration and corresponding adsorption energy of complexes containing multiple H_2O molecule clusters.

3.5. SAC enhances desulfurization reaction mechanism

Building upon both established literature and our experimental evidence, we systematically summarized and contrasted the desulfurization mechanisms between conventional AC and SAC, with the comparative analysis visually presented in Fig. 8.

The mechanism of AC desulfurization using the traditional activation method generally follows the theories of microporous adsorption and

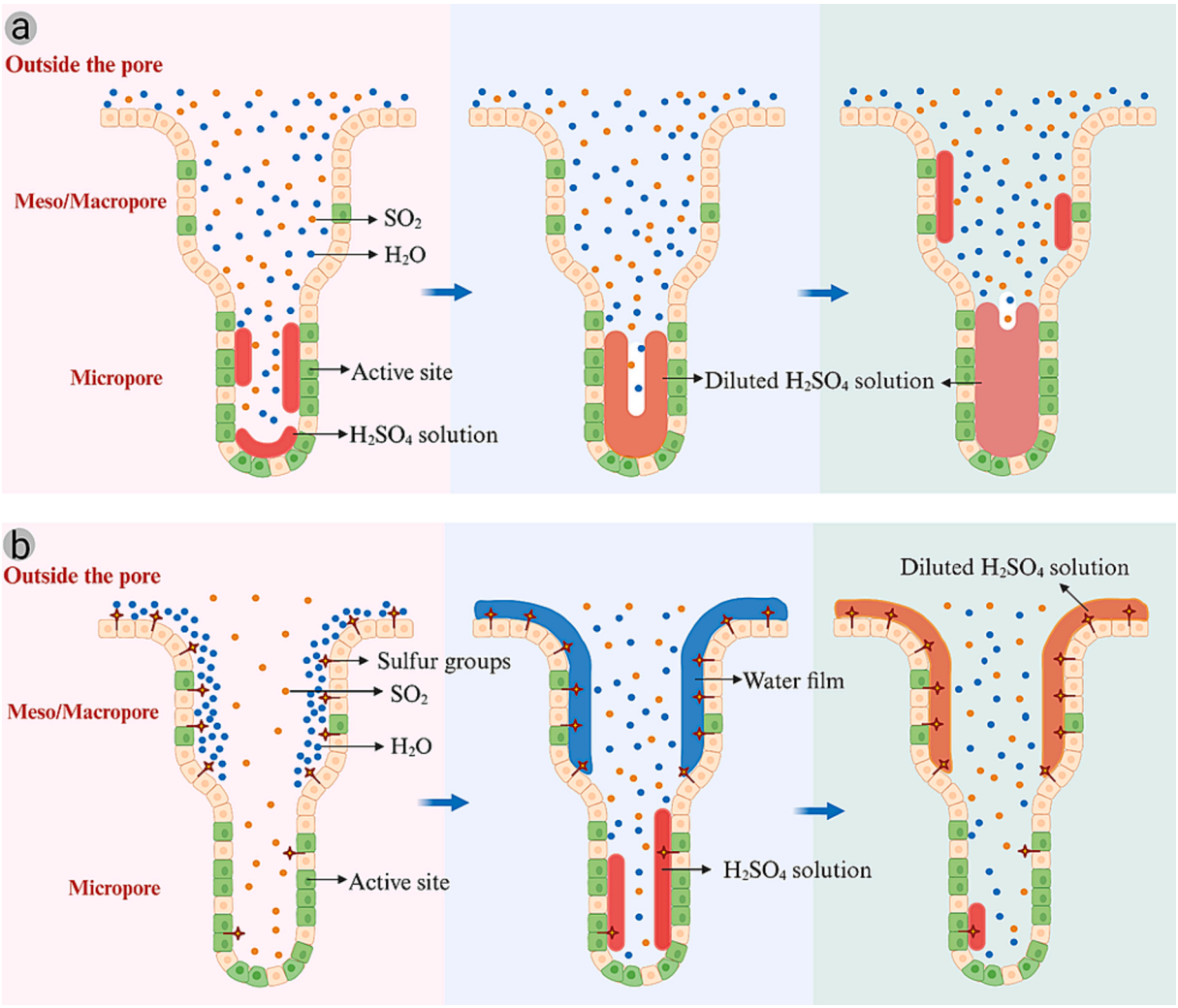

Fig. 8. Comparison of desulfurization mechanisms between (a) traditional AC and (b) SAC.

capillary condensation, as shown in Fig. 8a. First, during the diffusion and transport of gas molecules, SO_2 is primarily adsorbed onto the carbon framework within the microporous structure and oxidized under the catalytic action of the active sites. This reaction leads to the formation of H_2SO_4 when combined with H_2O. At this stage, the adsorption active sites and micropore volume are sufficient, corresponding to the initial stage of high removal efficiency in the SO_2 breakthrough curve (Fig. 3c) [8,48]. Second, as the reaction proceeded, the amount of H_2SO_4 increased, and combined with a large amount of H_2O to undergo capillary condensation and become an H_2SO_4 solution. The increased solution volume quickly occupied the micropores and active sites, leading to a rapid decline in desulfurization efficiency, which corresponded to a sharp increase in the SO_2 breakthrough curve [49,50]. Third, a minimal number of active sites in the mesopores and macropores continued to act, maintaining the desulfurization efficiency at a low level for a long time until complete deactivation, corresponding to the slow upward stage in the SO_2 breakthrough curve [51]. Therefore, the limited micropore volume and active site occupation are the main reasons for the low desulfurization efficiency of traditional AC.

For the SAC obtained by SO_2 activation (Fig. 8b), the sulfur-containing groups formed by sulfur doping changed the surface polarity of the carbon and exhibited hydrophilicity. First, in the initial adsorption stage, a higher concentration and smaller molecular size forced H_2O to rapidly diffuse and preferentially adsorb around sulfur-containing groups, gradually forming a water film as the molecules aggregated. SO_2 diffused to the microporous active sites but lacked the participation of H_2O, resulting in lower desulfurization efficiency, corresponding to the rising phase of the early SO_2 peak in Fig. 3a. Second, as the water film at the sulfur doping site gradually saturates, H_2O diffuses into the micropores to participate in desulfurization reactions and condenses into the H_2SO_4 solution, resulting in a significant increase in desulfurization efficiency, corresponding to the decreasing phase in the early SO_2 peak. Third, as the adsorption reaction proceeds, the nearly saturated H_2SO_4 filling the micropores comes into contact with the water film formed in the mesopores and macropores. Based on the concentration difference diffusion theory, it rapidly dilutes into mesopores and macropores. At this point, the micropores and active sites were released, demonstrating a relatively persistently high desulfurization efficiency, corresponding to the slow increase in the SO_2 concentration in the later stage. The entire strengthening effect gradually disappeared until the H_2SO_4 concentration in the mesopores and macropores was basically the same as that in the micropores, and the micropores and active sites were reoccupied, ultimately leading to deactivation of the adsorbent. Therefore, the hydrophilicity of the carbon induced by sulfur doping facilitates the migration of H_2SO_4 products, which is why SAC exhibits a high desulfurization performance and unique adsorption behavior.

4. Conclusions

This study demonstrates that carbothermal reduction of SO_2 at 800 °C simultaneously achieves high-yield elemental sulfur production

(>90.11 %) and fabricates SAC with exceptional desulfurization performance (a maximum sulfur capacity of 98.22 mg/g). The introduced sulfur groups significantly enhance SAC's surface hydrophilicity, endowing H_2O with competitive adsorption advantage over SO_2 at sulfur-functionalized sites. The synergistic modifications collectively facilitate H_2SO_4 migration from micropores and generate the distinctive saddle-shaped desulfurization profile. These findings establish a feasible strategy for converting pollutant SO_2 into enhanced carbon materials, which holds significant potential for simplifying existing AC-based flue gas desulfurization processes and improving system economics. Current limitations, including the need for precise control of sulfur doping sites within pore networks and long-term stability validation under industrial conditions, will direct future optimization toward scalable applications.

CRediT authorship contribution statement

Jun Li: Writing – original draft, Methodology, Conceptualization. **Xiang Wang:** Software, Investigation. **Xiao Zhu:** Validation, Resources. **Yuke Li:** Formal analysis. **Min Yan:** Writing – review & editing, Funding acquisition. **Yang Ma:** Investigation. **Ping Cui:** Software, Resources. **Jingcai Chang:** Writing – review & editing, Supervision. **Liqiang Zhang:** Visualization, Conceptualization. **Tao Wang:** Methodology. **Chunyuan Ma:** Funding acquisition. **Zhanlong Song:** Project administration.

Declaration of competing interest

The authors declare that they have no known competing financial interests or personal relationships that could have appeared to influence the work reported in this paper.

Acknowledgments

This work was supported by the Shandong provincial Natural Science Foundation (ZR2021ME049, ZR2023QE250), Taishan Industrial Experts Program (TSCX202306135), and National Natural Science Foundation of China (22478227).

Appendix A. Supplementary material

Supplementary data to this article can be found online at https://doi.org/10.1016/j.fuel.2025.136568.

Data availability

No data was used for the research described in the article.

References

[1] Zhang ZG, Xu C, Cheng G, Lau EV. Towards carbon neutrality: A comprehensive study on the utilization and resource recovery of coal-based solid wastes. Int J Coal Sci Technol 2025;12. Article 34.
[2] Sun F, Gao JH, Zhu YW, Chen GQ, Wu SH, Qin YK. Adsorption of SO_2 by typical carbonaceous material: a comparative study of carbon nanotubes and activated carbons. Adsorption 2013;19:959–66.
[3] Wu S, Wang WL, Ren CZ, Yao XL, Yao YG, Zhang QS, et al. Calcination of calcium sulphoaluminate cement using flue gas desulfurization gypsum as whole calcium oxide source. Constr Build Mater 2019;228:116676.
[4] Li J, Zhou BX, Chang JC, Chen SY, Ma CY, Zhang LQ, et al. Evolution of the physicochemical properties and SO_2 adsorption performance of powdered activated coke during adsorption–desorption cycle. J Anal Appl Pyrol 2022;167:105671.
[5] Feng T, Zhao XQ, Wang T, Xia X, Zhang MZ, Huan QC, et al. Reduction of SO_2 with CO to elemental sulfur in activated carbon bed. Energy Fuels 2016;30:6578–84.
[6] Guo YQ, Du ED. The effects of thermal regeneration conditions and inorganic compounds on the characteristics of activated carbon used in power plant. Energy Procedia 2012;17:444–9.
[7] Li B, Jiang HT, Zhang LQ, Wang ZQ, Ma CY. Adsorption equilibrium and kinetics of SO_2 on activated carbon. J China Coal Soc (China) 2012;10:1737–42.
[8] Sun F, Gao JH, Liu X, Tang XF, Wu SH. A systematic investigation of SO_2 removal dynamics by coal-based activated cokes: the synergic enhancement effect of hierarchical pore configuration and gas components. Appl Surf Sci 2015;357:1895–901.
[9] Zhu YW, Miao YF, Li HY. Enhancement effect of ordered hierarchical pore configuration on SO_2 adsorption and desorption process. Processes 2019;7. Article 173.
[10] Pi XX, Sun F, Qu ZB, Li Y, Gao JH. Hierarchical pore configuration in activated coke boosting direct desorption of desulfurization product H_2SO_4: a combined experimental and computational investigation. Fuel 2021;298:120697.
[11] Ma JR, Liu ZY, Liu SJ, Zhu ZP. A regenerable Fe/AC desulfurizer for SO_2 adsorption at low temperatures. Appl Catal B 2003;45:301–9.
[12] Tseng HH, Wey MY. Study of SO_2 adsorption and thermal regeneration over activated carbon-supported copper oxide catalysts. Carbon 2004;42:2269–78.
[13] Yang L, Jiang X, Jiang WJ, Wang PC, Jin Y. Cyclic regeneration of pyrolusite-modified activated coke by blending method for flue gas desulfurization. Energy Fuels 2017;31:4556–64.
[14] Ji PD, Gao X, Du XS, Zheng CH, Luo ZY, Cen KF. Relationship between the molecular structure of V_2O_5 /TiO_2 catalysts and the reactivity of SO_2 oxidation. Cat Sci Technol 2016;6:1187–94.
[15] Li J, Zhang LQ, Wang T, Chang JC, Song ZL, Ma CY. Study on sulfur migration in activated carbon adsorption-desorption cycle: effect of alkali/alkaline earth metals. J Environ Sci 2021;99:119–29.
[16] Long Y, Zhang CC, Wang XX, Gao JP, Wang W, Liu Y. Oxidation of SO_2 to SO_3 catalyzed by graphene oxide foams. J Mater Chem 2011;21. Article 13934.
[17] Cen WL, Hou ML, Liu J, Yuan SD, Liu YJ, Chu YH. Oxidation of SO_2 and NO by epoxy groups on graphene oxides: the role of the hydroxyl group. RSC Adv 2015;5:22802–10.
[18] Zhang HJ, Cen WL, Liu J, Guo JX, Yin HQ, Ning P. Adsorption and oxidation of SO_2 by graphene oxides: a van der Waals density functional theory study. Appl Surf Sci 2015;324:61–7.
[19] Qu ZB, Sun F, Gao JH, Pi XX, Qie ZP, Zhao GB. A new insight into SO_2 low-temperature catalytic oxidation in porous carbon materials: non-dissociated O_2 molecule as oxidant. Cat Sci Technol 2019;9:4327–38.
[20] Qu ZB, Sun F, Liu X, Gao JH, Qie ZP, Zhao GB. The effect of nitrogen-containing functional groups on SO_2 adsorption on carbon surface: enhanced physical adsorption interactions. Surf Sci 2018;677:78–82.
[21] Sun F, Gao JH, Liu X, Yang YQ, Wu SH. Controllable nitrogen introduction into porous carbon with porosity retaining for investigating nitrogen doping effect on SO_2 adsorption. Chem Eng J 2016;290:116–24.
[22] Yadav A, Dindorkar SS, Sinha N. Insights on the enhanced nitrogen dioxide sensing using doped boron nitride nanosheets through the quantum chemical studies. Chem Phys 2022;562:111629.
[23] Bi DM, Qiao L, Hu XY, Liu SJ. Geometrical and electronic structure investigations of S-doped graphene. Adv Mater Res 2013;669:144–8.
[24] Chen ZG, Deng BW, Du KF, Mao XH, Zhu H, Xiao W, Wang DH. Flue-gas-derived sulfur-doped carbon with enhanced capacitance. Adv Sustain Syst 2017;1. Article 1700047.
[25] Xia YD, Zhu YQ, Tang Y. Preparation of sulfur-doped microporous carbons for the storage of hydrogen and carbon dioxide. Carbon 2012;50:5543–53.
[26] Liu SY, Sun NQ, Li ZY, et al. Influence of process parameters of condensation on the recovery of SO_2 indesorption gas from flue gas adsorption desulfurization. Chin J Chem Eng 2020;71:5620–7.
[27] Pi XX, Sun F, Qu ZB, Gao JH, Wang AN, Zhao GB, et al. Producing elemental sulfur from SO_2 by calcium loaded activated coke: enhanced activity and selectivity. Chem Eng J 2020;401:126022.
[28] She M, Duan YF, Zhu C, Jia CQ. Impact of nonoxidized sulfur species on elemental mercury removal by SO_2 activated petroleum cokes. Energy Fuels 2020;34:14388–99.
[29] Li J, Chang JC, Cheng SJ, Wang ZA, Zhao Y, Zhou BX, et al. New insights into the influence of SO_2 as an activator on the physicochemical properties of carbon materials and the influence of S-doping on SO_2 adsorption: experimental and density functional theory study. Chem Eng J 2023;474:145902.
[30] Grimme S, Antony J, Ehrlich S, Krieg H. A consistent and accurateab initio parametrization of density functional dispersion correction (DFT-D) for the 94 elements H-Pu. J Chem Phys 2010;132:154104.
[31] Lu T, Chen FW. Multiwfn: a multifunctional wavefunction analyzer. J Comput Chem 2012;33:580–92.
[32] Humphrey W, Dalke A, Schulten K. VMD: visual molecular dynamics. J Mol Graph 1996;14:33–8.
[33] Yu Y, Zhao RH, Li XY, Chen J, Dong Y. Mechanism of CaO and Fe_2O_3 capture gaseous arsenic species in the flue gas: DFT combined thermodynamic study. Fuel 2022;312:122838.
[34] Humeres E, Peruch MDGB, Moreira RFPM, Schreiner W. Reactive intermediates of the reduction of SO_2 on activated carbon. J Phys Org Chem 2003;16:824–30.
[35] Li XH, Sun F, Qu ZB, Feng YP, Li Y, Yang CL, et al. Selective pore regulation of activated carbon using trace carbonate-assisted catalytic activation: revealing the effect of cation catalysis on pore topology. Chem Eng J 2024;481:148626.
[36] Gan XW, Chen ZJ, Ma WH, Xie R, Luo P. Study on the synergistic effect of co-pyrolysis gasification of low-grade non-cohesive coal and waste biomass. Fuel 2025;381:133569.
[37] Gan XW, Chen ZJ, Ma WH, Wang XY. A study on composite carbonaceous reducing agent pellets based on low-order unbonded coal. Fuel 2024;371:131947.
[38] Yu X, Park HS. Sulfur-incorporated, porous graphene films for high performance flexible electrochemical capacitors. Carbon 2014;77:59–65.
[39] Gan XW, Chen ZJ, Ma WH, et al. A new type of carbonaceous reducing agent pellets for industrial silicon smelting with low grade non-stick coal coupled micro-silicon

powder: from laboratory scale to industrial test scale. J Clean Prod 2025;516:145829.
[40] Zhu MQ, Yan QT, Duan YF, Li J, Zhang X, Han ZX, et al. Study on preparation and mercury adsorption characteristics of columnar sulfur-impregnated activated petroleum coke. Energy Fuels 2020;34:10740–51.
[41] Cheng G, Li YL, Cao YJ, Zhang ZG. A novel method for the desulfurization of medium-high sulfur coking coal. Fuel 2023;335:126988.
[42] Wang JX, Meng XR, Chen JS, Yu YK, Miao JF, Yu WJ, et al. Desulphurization performance and mechanism study by in situ DRIFTS of activated coke modified by oxidization. Ind Eng Chem Res 2016;55:3790–6.
[43] Marques SCR, Marcuzzo JM, Baldan MR, Mestre AS, Carvalho AP. Pharmaceuticals removal by activated carbons: role of morphology on cyclic thermal regeneration. Chem Eng J 2017;321:233–44.
[44] Cheng G, Zhang MN, Zhang YH, Lin B, Zhan HJ, Zhang HJ. A novel renewable collector from waste fried oil and its application in coal combustion residuals decarbonization. Fuel 2022;323:124388.
[45] Humeres E, Debacher NA, Moreira RDFP, Santaballa JA, Canlel M. Reactive site model of the reduction of SO_2 on graphite. J Phys Chem C 2017;121:14649–57.
[46] Zhou BX, Wang T, Xu TM, Li C, Li J, Fu JP, et al. Comparative study on the preparation of powdered activated coke for SO_2 adsorption: One-step and two-step rapid activation methods. Fuel 2020;4:119570.
[47] Zhang Z, Wang T, Pan XH, Zhou BX, Ma CY. Effect of temperature on pore structure evolution during powder-activated coke preparation by flue gas activation. J China Coal Soc 2019;44:3564–70.
[48] Chen EY, Jia LJ, Jia XB, Wei QY, Zhang L. Understanding the adsorption and separation of sulfur dioxide in flue gas by Zeolitic imidazolate frameworks via molecular simulation. Chem Phys Lett 2021;778:138788.
[49] Gaur V, Asthana R, Verma N. Removal of SO_2 by activated carbon fibers in the presence of O_2 and H_2O. Carbon 2006;44:46–60.
[50] Hazra MK, Sinha A. Formic acid catalyzed hydrolysis of SO_3 in the gas phase: a barrierless mechanism for sulfuric acid production of potential atmospheric importance. J Am Chem Soc 2011;133:17444–53.
[51] Zhang MZ. Study on SO_2 adsorption by powdery activated coke in turbulent fluidized bed and process intensification. Jinan: Shandong University; 2022.